PHILOSOPHICAL TRANSACTIONS A

royalsocietypublishing.org/journal/rsta

Research

**Cite this article:** Cooper VT, Roach LA, Thomson J, Brenner SD, Smith MM, Meylan MH, Bitz CM. 2022 Wind waves in sea ice of the western Arctic and a global coupled wave-ice model. *Phil. Trans. R. Soc. A* **380**: 20210258. https://doi.org/10.1098/rsta.2021.0258

Received: 11 March 2022
Accepted: 12 July 2022

One contribution of 17 to a theme issue 'Theory, modelling and observations of marginal ice zone dynamics: multidisciplinary perspectives and outlooks'.

**Subject Areas:**
climatology, oceanography, atmospheric science

**Keywords:**
sea ice, ocean waves, marginal ice zone, coupled wave-ice model, field observations, wave attenuation

**Author for correspondence:**
V. T. Cooper
e-mail: vcooper@uw.edu

†Now at NASA Goddard Institute for Space Studies and Center for Climate Systems Research, Columbia University, New York City, NY, USA.

Electronic supplementary material is available online at https://doi.org/10.6084/m9.figshare.c.6135513.

THE ROYAL SOCIETY PUBLISHING

# Wind waves in sea ice of the western Arctic and a global coupled wave-ice model

V. T. Cooper[1], L. A. Roach[1,†], J. Thomson[2], S. D. Brenner[2], M. M. Smith[2], M. H. Meylan[3] and C. M. Bitz[1]

[1]Department of Atmospheric Sciences, University of Washington, Seattle, WA 98195, USA
[2]Applied Physics Laboratory, University of Washington, Seattle, WA 98105, USA
[3]School of Information and Physical Sciences, The University of Newcastle, Callaghan, New South Wales 2308, Australia

VTC, 0000-0001-9697-1992; LAR, 0000-0003-4189-3928; JT, 0000-0002-8929-0088; SDB, 0000-0002-0826-1294; MMS, 0000-0003-2259-042X; MHM, 0000-0002-3164-1367; CMB, 0000-0002-9477-7499

The retreat of Arctic sea ice is enabling increased ocean wave activity at the sea ice edge, yet the interactions between surface waves and sea ice are not fully understood. Here, we examine *in situ* observations of wave spectra spanning 2012–2021 in the western Arctic marginal ice zone (MIZ). Swells exceeding 30 cm are rarely observed beyond 100 km inside the MIZ. However, local wind waves are observed in patches of open water amid partial ice cover during the summer. These local waves remain fetch-limited between ice floes with heights less than 1 m. To investigate these waves at climate scales, we conduct experiments varying wave attenuation and generation in ice with a global model including coupled interactions between waves and sea ice. A weak high-frequency attenuation rate is required to simulate the local waves in observations. The choices of attenuation scheme and wind input in ice have a remarkable impact on the extent of wave activity across ice-covered oceans, particularly in the Antarctic. As well as demonstrating the need for stronger constraints on wave attenuation, our results suggest that further

attention should be directed towards locally generated wind waves and their role in sea ice evolution.

This article is part of the theme issue 'Theory, modelling and observations of marginal ice zone dynamics: multidisciplinary perspectives and outlooks'.

## 1. Introduction

As sea ice retreats and exposes larger open-water areas in the Arctic Ocean, interactions between ocean surface waves and sea ice may play an elevated role in the Arctic climate system [1]. Wave-ice interactions typically occur in the marginal ice zone (MIZ), the partially ice-covered region that separates interior pack ice from open ocean. The fracture of sea ice by ocean surface waves in the MIZ may affect regional climate feedbacks through enhanced sea ice melt (e.g. [2]) motivating the development of fully coupled wave-ice models in recent years (e.g. [3,4]).

However, significant uncertainty remains in our understanding of fundamental aspects of wave-ice physics [5,6]. A major obstacle is that observations of waves in polar oceans are rare and hard to obtain, and existing *in situ* datasets sample a limited range of ocean and sea ice conditions [7]. Despite recent progress (e.g. [8–10]), comprehensive datasets from remote sensing are not yet available. These observing challenges leave us with only weak constraints on the ocean surface wave climate in sea ice.

Swell, low-frequency ocean surface waves that have developed in open ocean areas, can propagate into the MIZ and decay with distance inside the sea ice edge. Many studies have considered the attenuation of swell waves in sea ice, but the theory has not yet converged on a definitive explanation [11]. A wide variety of attenuation schemes have been proposed based on different theoretical frameworks and observations [12–14], and their respective impacts on wave climate have not yet been systematically investigated.

Besides propagation of swell, ocean surface waves may also be generated inside the sea ice edge by local winds. In contrast to the large body of work on the attenuation of swell and its incorporation into numerical models, less focus has been directed toward these high-frequency wind waves. According to [15], wind waves tend to dissipate during their first 10–20 km of travel into the sea ice field. However, in [16] a model was developed explaining how local wind waves can be generated anew in areas of low sea ice concentration (SIC) and sparse ice floes. Using surface buoy measurements, [17] found support for the open-water distance between floes as a control parameter for local wave energy. We are not aware of theories that explain how wind input for wave growth is modified in partial ice cover. The simple assumption in current wave models scales the wind input by the open-water fraction [18]. The importance of local wind-wave generation in partial ice cover for Arctic climate remains unclear.

Here, we leverage multi-year *in situ* observations from two recent field campaigns in the Western Arctic: the Beaufort Gyre Observing System (BGOS) and Stratified Ocean Dynamics in the Arctic (SODA). In contrast to previous case studies, these data from subsurface moorings offer a long-term view of fundamental properties of waves in ice. We examine the significant wave heights, the wave spectra, and the prevalence of wind waves and swell in observations. We aim to explore whether and how small-scale processes captured in these observations might play a role in large-scale Arctic and Antarctic climate. We use a global coupled wave-ice model [3] (with a spatial resolution of 50 km) to simulate spectra and to quantify the extent of sea ice affected by ocean surface waves. We investigate how this quantity and how wave spectra in ice are affected by uncertainty in wave-ice physics, and our results highlight specific areas that should be addressed in the development of climate-scale coupled wave-ice models.

The paper begins with descriptions of observations from BGOS and SODA in §2a and the coupled wave-ice model in §2b. We present results from the observations grouped by distance inside the ice edge in §3a. In §3b we compare results from wave-ice model sensitivity experiments with observations, and in §3c we explore how varying wave-ice physics affects the wave climate

**Table 1.** Summary of *in situ* observations.

| dataset | instrument | period | lat., lon. | open water[a] | 0–100 km[a] | > 100 km[a] |
|---|---|---|---|---|---|---|
| BGOS-A | AWAC | 2012–21 | 75 N, 150 W | 5796 | 54 | 70 |
| BGOS-D | AWAC | 2013–20 | 74 N, 140 W | 2481 | 131 | 6 |
| SODA-A | Signature500 | 2018–19 | 73 N, 148 W | 1096 | 39 | 10 |
| SODA-B | Signature500 | 2018–19 | 75 N, 146 W | 314 | 97 | 1 |
| SODA-C | Signature500 | 2018–19 | 78 N, 139 W | 0 | 0 | 11 |
| BGOS-SODA total | | | | 9687 | 321 | 98 |

[a]Count of valid wave measurements in sample with significant wave height exceeding the 0.3 m approximate detection limit; data are grouped by distance inside the ice edge ($\Delta^{\text{dist}}$), defined in §2c.

in sea ice across each hemisphere. In §4, we discuss implications for seasonal ice melt and future modelling efforts. We conclude in §5.

## 2. Methods

### (a) *In situ* observations

We use subsurface-mooring observations obtained from two separate field campaigns:

(i) BGOS [19] includes two subsurface moorings with upward-looking Nortek Acoustic Wave and Current (AWAC) instruments for surface tracking. BGOS-A and BGOS-D sample every hour and began collecting measurements in 2012 and 2013, respectively. Raw data are processed into wave spectra following [20–22] as in [1,17]. BGOS data are mostly continuous from 2012 to 2021 [23].

(ii) SODA includes three subsurface moorings using the upward-looking Nortek Signature Doppler profiler for acoustic surface tracking. Raw data from SODA are quality-controlled using methods comparable to the BGOS methods, producing measurements of surface wave spectra sampled every 2 h. SODA data span 2018–2019 [24].

The aggregate dataset (denoted as BGOS-SODA) spans 2012–2021 and five locations in the central Beaufort Sea (table 1 and figure 1). Both sets of subsurface moorings detect surface gravity waves via altimeter measurements of surface displacement. A nuance of the moorings (compared with surface buoys, for example) is that the moorings' surface tracking simultaneously measures surface gravity waves and sea ice draft. The spectral signal from surface waves can be distinguished from that of the sea ice bottom during the quality-control process—additional details are included in the electronic supplementary material, §S8—ensuring that the ocean wave data represent surface waves, not ice draft.

### (b) Coupled wave-ice model experiments

We conduct a series of experiments using the CICE5 sea ice model [27], coupled by Roach *et al*. [3] to the WAVEWATCH III® v. 5.16 ocean-surface-wave model (WW3) [28]. Instead of taking prescribed ice conditions as input and only predicting the waves (as in operational wave forecasts), both the ice and the wave conditions are freely evolving on a global domain. The global coupled wave-ice model is forced by the JRA-55 atmospheric reanalysis [29,30] and coupled to a slab ocean model [31], which includes annually periodic ocean surface currents. CICE5 is modified to treat the joint floe size and thickness distribution (FSTD) as in [3,32]. The integral of the FSTD over all thicknesses is the floe size distribution, which evolves prognostically subject

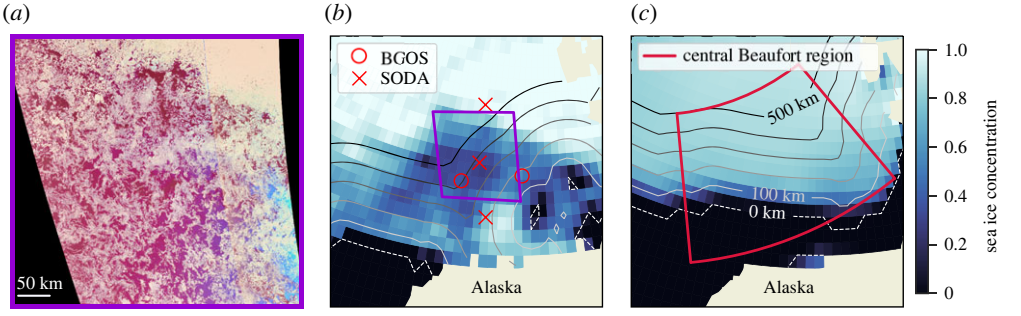


**Figure 1.** (*a*) Synthetic aperture radar (SAR) [25,26] from 28 July 2018 showing ice floes (in off-white) in the central Beaufort Sea during the summer melt, corresponding to the purple box marked in *b*. (*b*,*c*) SIC (colour shading) and corresponding distance inside the ice edge ($\Delta^{\text{dist}}$, contour lines every 100 km from 0 to 500 km) on the same day from (*b*) passive microwave satellite observations and (*c*) the coupled wave-ice model (FSD-M21 case). The 0 km-distance contour denotes 15% SIC. Red symbols in *b* show locations of *in situ* observations. Red box in *c* shows the region we define as the central Beaufort region for analysing model output. (Online version in colour.)

to lateral growth and melt, welding of floes in freezing conditions, wave-induced floe fracture (following [33]) and wave-dependent new ice formation [3,32].

The sea ice and wave models are on a displaced-pole nominal 1° grid (gx1v7), and the size of model grid cells near observations in the Beaufort Sea is approximately 50 km × 50 km. This model is the same as FSD-WAVEv2 in [3], except that (i) we use a higher wave-ice coupling frequency, exchanging the wave spectrum and SIC, thickness, and mean floe size every hour to better resolve short-time-scale wave-ice interactions; (ii) we modify the numerical approach such that the source term for wave-ice interactions in WW3, $S_{\text{ice}}$, is applied alongside the other source terms without time-splitting (which appears to be impactful for the nominal 1° resolution); and (iii) we use WIFF1.0 [34] for floe fracture, which is a computationally efficient version of the parametrization in [33] developed using machine learning. In WW3, the global timestep is set to 1800 s, the spatial propagation is set to 600 s, the intra-spectral propagation is set to 1800 s, and the minimum source-term step is set to 20 s. The model spin-up period covers 2000–2018, and sensitivity experiments with varied attenuation schemes are run for one year each, branched from the spin-up at 1 January 2018. We analyse hourly output from 2018, which is during the BGOS-SODA observing period and enables comparisons to be made between the model and observations from the western Arctic.

The experiments (table 2) test a wide range of attenuation rates $\alpha$ that vary in how they depend on frequency and on wave-ice attributes ($\alpha$ is illustrated in the electronic supplementary material, figure S1). We test the six IC4 attenuation methods included in WW3 [28,39], as well as the attenuation scheme used by Roach *et al*. [3], denoted as FSD-M21. FSD-M21 is an empirical fit to the floe-scattering theory of [41] with supplemental dissipation for long wavelengths, and it depends on mean floe size and mean ice thickness. We use FSD-M21 during model spin-up. The attenuation schemes tested here are not exhaustive. WW3 includes schemes outside of the IC4 framework (such as IC2+IS2 [43,44]), and there are others (e.g. [45]) not yet in WW3 that could be tested in future versions of the model.

By default, the wave source terms in WW3 v. 5.16 are scaled by the open-water fraction, 1 − SIC. This default scaling reduces the source to zero when SIC = 100%. Because the effect of ice cover on wind input $S_{\text{in}}$ is uncertain, we run two sets of experiments: one that uses the default scaling and another that allows some wind input to persist when the SIC reaches 100%. The 'enhanced wind input' experiments scale $S_{\text{in}}$ by 1 − SIC/2, which forces $S_{\text{in}}$ to go from its full value to half-strength as SIC goes from zero to 100%. The 'enhanced wind input' is not a physically plausible parametrization, but it provides a hypothetical upper bound on the potential

**Table 2.** Summary of model experiments (varying attenuation rates).

| experiment | $\alpha$: $T = 2.5$ s[a] | reference | $\alpha$ dependencies |
|---|---|---|---|
| IC4M1 | $4 \times 10^{-4}$ | [35] | period only as exponential function |
| IC4M2 | $2 \times 10^{-3}$ | [36] | period only as fourth-degree polynomial |
| IC4M3rad1 | $2 \times 10^{-1}$ | [33,37] | period; ice thickness[b] |
| IC4M4 | $1 \times 10^{-5}$ | [38] | depends only on significant wave height ($H_s$) |
| IC4M5 | $2 \times 10^{-4}$ | [39] | period only as piecewise step function (electronic supplementary material, figure 1) |
| IC4M7 | $1 \times 10^{-2}$ | [40] | period; ice thickness |
| FSD-M21 | $5 \times 10^{-3}$ | [41] | period; mean floe radius, mean ice thickness |

[a] Attenuation rate $\alpha$ at high-frequency reference of 0.4 Hz (period $T = 2.5$ s), thickness 0.5 m, significant wave height $H_s = 1.0$ m (for IC4M4) and floe radius 100 m (for FSD-M21).

[b] $\alpha$ varies with floe size in [33] but has a constant floe radius of 1.0 m specified in WW3 [42].

impact of wind input in ice-covered seas. In all experiments, we maintain the default scaling on the nonlinear source, $S_{\mathrm{nl}}$ (see discussion in [46,47]). WW3 also includes a linear source $S_{\mathrm{ln}}$ that supports initial wave growth. In all experiments, we remove any scaling on $S_{\mathrm{ln}}$ to allow new wave growth in ice. This decision is based on observations of local waves inside the ice edge, which are described in §3a.

### (c) Distance inside the ice edge

To enable comparison between observations and the wave-ice model with climate-scale resolution, we group wave data based on distance inside the ice edge, $\Delta^{\mathrm{dist}}$, defined here as the haversine distance to the nearest ocean grid cell with SIC less than 15%. Note that $\Delta^{\mathrm{dist}}$ does not directly represent the distance along which wave attenuation occurs. The distance into the ice that a wave will travel before full dissipation depends on its direction of propagation, whereas $\Delta^{\mathrm{dist}}$ quantifies the separation from open ocean. For simplicity, we show three $\Delta^{\mathrm{dist}}$ groups: open water (SIC < 15%), 0–100 km $\Delta^{\mathrm{dist}}$ (equivalent to approximately two 50 km × 50 km model grid cells) and >100 km $\Delta^{\mathrm{dist}}$. We estimate $\Delta^{\mathrm{dist}}$ for each *in situ* observation using the NOAA/NSIDC climate data record (CDR) of SIC, a daily satellite product from passive microwave observations [48–50]. We interpolate the CDR observations to the model grid. In using $\Delta^{\mathrm{dist}}$ for our analysis, we aim to describe the large-scale transition from open ocean to pack ice (rather than resolve individual leads or small-scale patches of open water).

## 3. Results

### (a) Observed wave spectra in the Beaufort Sea

We begin by considering the distribution of significant wave height, $H_s$, in the BGOS-SODA dataset (figure 2*a–c*). In open water (SIC < 15%, figure 2*a*), there is a maximum $H_s$ of 4.2 m and a peak occurrence between 0.5 m and 0.7 m. Approximately half of the open-water observations have $H_s$ exceeding 1.0 m. Note that we have not controlled for distance outside of the ice edge; some observations are made where SIC is small but non-zero, while others are very far from any sea ice. At 0–100 km $\Delta^{\mathrm{dist}}$ (figure 2*b*), the distribution has a thicker tail and a maximum $H_s$ at 3.6 m. The peak occurrence is between 0.3 m and 0.5 m, where the lower bound is at the detection limit. Approximately one-third of the 0–100 km $\Delta^{\mathrm{dist}}$ observations have $H_s$ exceeding 1.0 m. Beyond a $\Delta^{\mathrm{dist}}$ of 100 km (figure 2*c*), the distribution peaks between 0.4 m and 0.6 m. No observations exceed 1.0 m $H_s$ at $\Delta^{\mathrm{dist}} > 100$ km. While it is conceivable that the mooring altimeters could fail

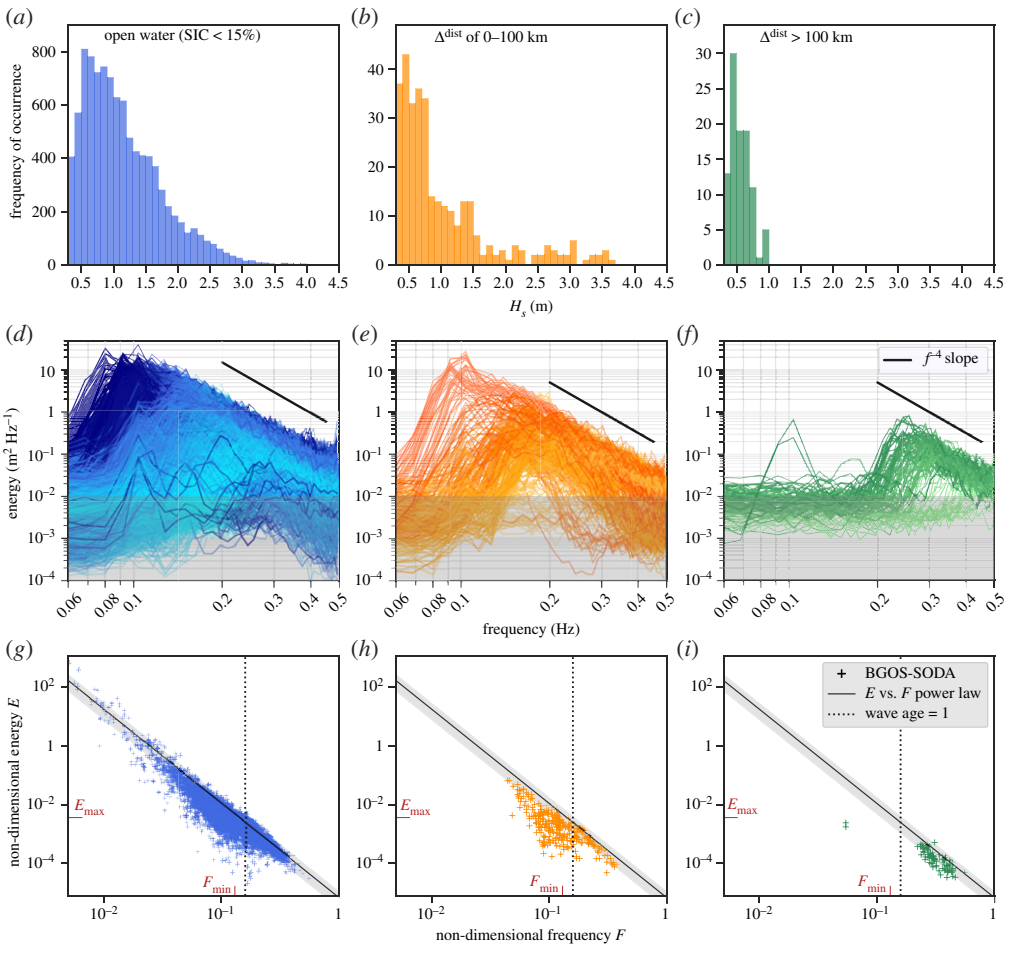


**Figure 2.** Wave properties in observations from the aggregate BGOS-SODA dataset in the Beaufort Sea, grouped by $\Delta^{\text{dist}}$ column-wise. (*a–c*) Histograms of significant wave height $H_s$, (*d–f*) wave spectra, and (*g–i*) non-dimensional scaling of energy $E$ versus frequency $F$. Wave spectra in *d–f* are coloured by peak frequency as a visual aid. In (*g–i*), the power law (black line) of $E$ versus $F$ for wind-generated, fetch-limited waves is shown with confidence intervals, and the fully developed limit ($E_{\text{max}}$, $F_{\text{min}}$) for pure wind seas [51] is indicated in red. The dashed line at $F = (2\pi)^{-1}$ indicates wave age = 1, and wave age increases to the left (as $F$ decreases). Only spectra with $H_s > 0.3$ m, the approximate detection limit of the moorings, are included in all panels. Grey shading in *d–f* below $10^{-2}$ also represents the approximate detection limit. (Online version in colour.)

to capture some of the smallest waves near the detection limit, it is unlikely that the instruments would miss recording large wave heights that exceed 1.0 m.

Turning to the wave energy spectra (figure 2*d–f*), there are pronounced contrasts between the open-water spectra and those from inside the sea ice edge. The open-water spectra (figure 2*d*) exemplify a characteristic power-law relationship between energy and frequency in the high-frequency spectral tail, i.e. the tail generally follows a consistent $f^{-4}$ slope above the peak frequency, $f_p$. Some bimodal spectra are discernible with swell peaks near 0.1 Hz and separate high-frequency peaks from local winds. Data from the 0–100 km $\Delta^{\text{dist}}$ transition into ice (figure 2*e*) appear to mostly have spectral tails with slopes steeper than $f^{-4}$. This steeper slope is typical for waves in sea ice [46,52], consistent with the notion that sea ice dissipates high-frequency energy most effectively. This phenomenon is illustrated more clearly by supplemental surface buoy spectra (electronic supplementary material, figure S2) in a separate dataset from the Arctic Sea State [53].

The dominant wave mode beyond 100 km $\Delta^{\text{dist}}$ has a spectral signature that is unexpectedly reminiscent of the open-water spectra, although with shorter wave periods. This wave mode has all energy at high frequencies, and the spectral tails appear to follow the $f^{-4}$ slope. Only two spectra across the BGOS-SODA dataset at $\Delta^{\text{dist}} > 100$ km have $f_p$ lower than 0.2 Hz. The presence of high-frequency energy far inside the ice edge is unexpected, given that sea ice is understood to quickly dissipate high-frequency energy [15,46,52].

We next determine whether a spectrum is described by local wind-wave generation or is dominated by swell using non-dimensional scaling of bulk wave parameters (see appendix A, following [51]). Fetch-limited wave generation by local winds is expected to produce waves that follow an empirical power law, equation (A 4), relating non-dimensional energy $E$ to frequency $F$, where $E \propto H_s^2$ and $F \propto f_p$. Local wind waves are also expected to have a wave age $c/U$ that is less than 1, where $c$ is the phase speed at $f_p$ and $U$ is the 10 m wind speed. In open water (figure 2*g*), there are many observations that meet these wind-wave criteria. There are also many observations that fall below the $E$ versus $F$ line and have transitioned to wave age greater than 1 (indicating swell). At 0–100 km $\Delta^{\text{dist}}$ in figure 2*h*, we can see that some spectra still follow local wind generation, but a large cluster of data moves into the swell mode, falling below the power law and towards greater wave age. The most distinct result is in figure 2*i* at $\Delta^{\text{dist}} > 100$ km, where the data overwhelmingly follow the power law for local wind waves, and only two outlier spectra resemble swell.

We also use an alternative approach to validate that the observations at $\Delta^{\text{dist}} > 100$ km are local wind waves. This approach uses the wave spectra to estimate the local wind speed (see appendix B, following [54,55]), whereas the non-dimensional scaling for $E$ and $F$ employed the 10 m wind speed ($U_{10}$) from JRA reanalysis. We compare estimates of $U_{10}$ from the BGOS-SODA measurements with local wind speeds from JRA in figure 3. If $U_{10}$ values predicted from BGOS-SODA wave spectra match $U_{10}$ values from reanalysis, this implies that the observed waves are generated by local winds. When assuming the reanalysis to be truth, wave-based estimates of $U_{10}$ from $\Delta^{\text{dist}} > 100$ km have (i) root-mean-square error (RMSE) of 2.2 m s$^{-1}$ for winds less than 12 m s$^{-1}$ and (ii) relative error of 18% for winds greater than 10 m s$^{-1}$. Open-water observations have (i) RMSE of 2.2 m s$^{-1}$ for winds less than 12 m s$^{-1}$ and (ii) relative error of 16% for winds greater than 10 m s$^{-1}$. These statistics are quite close to those reported in [55], despite the possible inaccuracy in using re-analysis as truth in this study. To obtain these results, a different directional spreading parameter, $I_p$, is used in ice and in open water, as noted in appendix B. The wind-speed estimation provides additional evidence that the spectra from $\Delta^{\text{dist}} > 100$ km represent waves generated by local winds.

Finally, we consider the implied fetch that is consistent with each observed wind-wave spectrum. In figure 4, we estimate an implied fetch based on the fetch-limited scaling relations (as described in appendix A, following [51]). Fetch estimates can be calculated from either the non-dimensional energy $E$ or the frequency $F$ in the BGOS-SODA measurements—differences between the two fetch estimates correspond to scatter or bias relative to the power law in figure 2*i*. Both estimates indicate that the majority of observed wind waves from beyond 100 km $\Delta^{\text{dist}}$ require less than 20 km of open-water fetch, and all measurements require less than 40 km. We do not have colocated SAR images at times of the moorings' wave measurements from beyond 100 km $\Delta^{\text{dist}}$, but SAR images from 18 July 2018 (two days prior to BGOS-A and BGOS-D wind-wave observations) show open-water patches with length scales of $O(10)$ km (figure 5). Wind waves could arise in these open-water areas just as short waves develop in large lakes. The apparent fetch in figure 5 from before (18 July 2018), near when (25 July 2018) and after (28 July 2018) local waves were reported appears broadly consistent with the implied fetch estimates in figure 4.

In summary, multi-year observations from a seasonal ice zone in the Beaufort Sea reveal that at distances beyond 100 km inside the sea ice edge, (i) there are no records of $H_s > 1.0$ m, (ii) there is a peak in the frequency of occurrence of $H_s$ near 0.5 m, and (iii) nearly all of the observed waves are generated by local winds rather than swell propagating into sea ice. The observations also show swell waves in the first 0–100 km of ice, and the maximum $H_s$ in open water is 4.2 m. We next

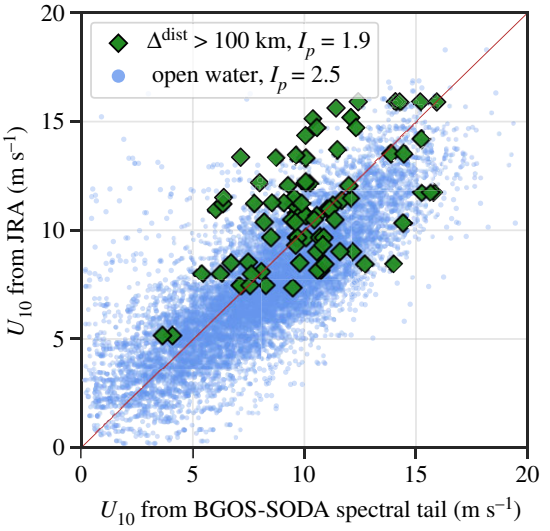


**Figure 3.** Ten-metre wind speed from (vertical axis) JRA reanalysis and (horizontal axis) estimates using BGOS-SODA surface wave spectra. Spectra are measured using upward-looking altimeters on moorings located 30–45 m beneath the ocean surface; $I_p$ is an assumed constant representing directional spreading of waves and is used to estimate $U_{10}$ from BGOS-SODA data. See appendix B for details of estimating $U_{10}$ from wave spectra. (Online version in colour.)

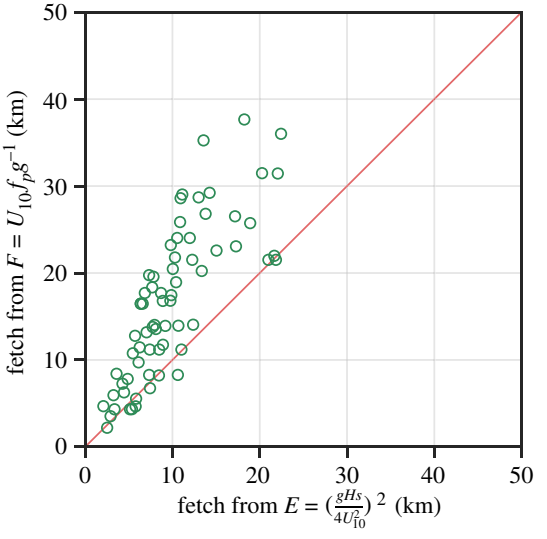


**Figure 4.** Implied fetch for locally generated wind waves from BGOS-SODA observations at $\Delta^{dist} > 100$ km. The vertical axis indicates estimates based on non-dimensional frequency $F$, and the horizontal axis indicates corresponding estimates based on non-dimensional energy $E$. The 50 km $\times$ 50 km axes represent approximate model resolution in the Beaufort Sea. (Online version in colour.)

consider whether these characteristics can be captured in a global climate-scale coupled wave-ice model.

## (b) Simulated wave spectra in the Beaufort Sea

We now investigate how variations in wave-ice physics influence the simulation of ocean surface waves in the presence of sea ice, with particular attention to reproducing the spectral shape of

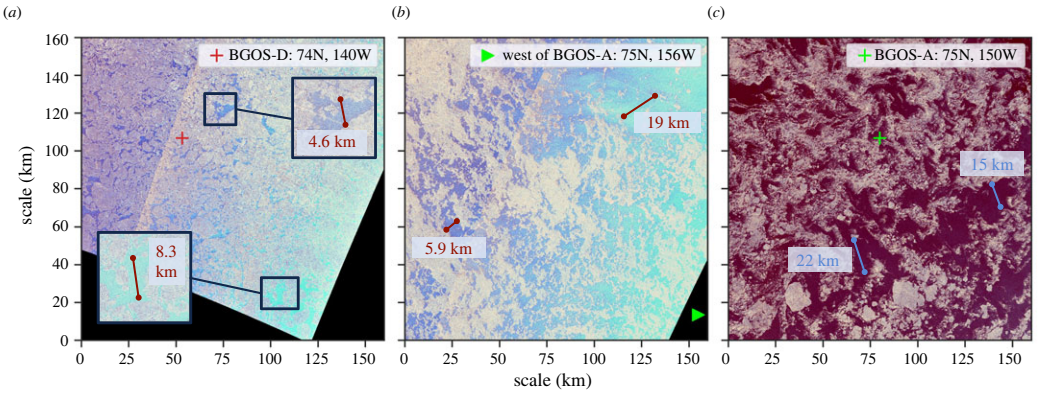


**Figure 5.** SAR images in the Beaufort Sea from (*a*) 18 July 2018 located over BGOS-D (east of BGOS-A), (*b*) 25 July 2018 (160 km west of BGOS-A) and (*c*) 28 July 2018 located over BGOS-A. Sea ice is shown in off-white colour [25,26]. Annotations show sample fetch estimates in the direction of local surface winds. (Online version in colour.)

observed wind waves in partial ice (figure 2*f*). At the model resolution (50 km, which is larger than the estimated fetch required for the observed wind waves), it is not possible to resolve the small-scale processes that occur in reality. Given this resolution limitation for climate-scale modelling, we rather seek to understand the balance between wind input ($S_{in}$), attenuation by ice ($S_{ice}$) and scaling by SIC that results in wave spectra which best match the BGOS-SODA observations.

Figure 6 shows model results from the central Beaufort Sea during July, the month in which the vast majority of wind-wave observations at $\Delta^{dist} > 100$ km in BGOS-SODA occur (electronic supplementary material, figure S4*c*). Experiments IC4M3rad1 and IC4M7 have no spectra with $H_s > 0.1$ m where SIC exceeds 15% in July 2018, so these experiments are omitted from figure 6.

We first focus on the high-frequency portion of the spectrum. Across the model experiments, IC4M1 (figure 6*a*,*b*) agrees most closely with the Beaufort Sea observations (figure 2*f*) in that its dominant wave mode at $\Delta^{dist} > 100$ km corresponds to the short wind waves. The agreement with observations is particularly strong in the experiment that allows substantial wind input even when SIC is high (figure 6*b*). Notably, IC4M1 is neither new nor complex. It is a simple exponential function of period based on field experiments published in 1988 [35]. IC4M5 also has a wind-wave spectral signature in the high frequencies (figure 6*g*,*h*). The FSD-M21 experiments damp all $H_s$ to less than 0.3 m before the waves reach 100 km $\Delta^{dist}$ (not shown), and the spectra from the first 0–100 km demonstrate that high-frequency energy is eliminated rapidly in ice (figure 6*i*). With FSD-M21, allowing additional wind input has minimal impact on the simulated spectra (figure 6*j*). The results for IC4M3rad1 and IC4M7 (not shown), which both depend on ice thickness, have even stronger damping than FSD-M21.

Turning to the low-frequency portion of the spectrum, many of the experiments appear to have too much low-frequency energy in ice because observations show little evidence of swell beyond 100 km inside the MIZ. IC4M1 is a notable exception in that its spectra at $\Delta^{dist} > 100$ km show lower levels of swell. IC4M2, IC4M4 and IC4M5 all have much higher energy in the low-frequency range than we see in observations. Note that spectra from IC4M5 show abrupt jumps in energy because $\alpha$ is a piecewise (not smooth) function in that case (electronic supplementary material, figure S1). FSD-M21 also favours the low frequencies, showing swell spectra at 0–100 km $\Delta^{dist}$ that have similarities to some observations in figure 2*e*, although most of those observations are from October rather than July (electronic supplementary material, figure S4*b*). The low-frequency attenuation rate may need to be stronger than that of IC4M2, IC4M4 and IC4M5 to improve comparison with observations.

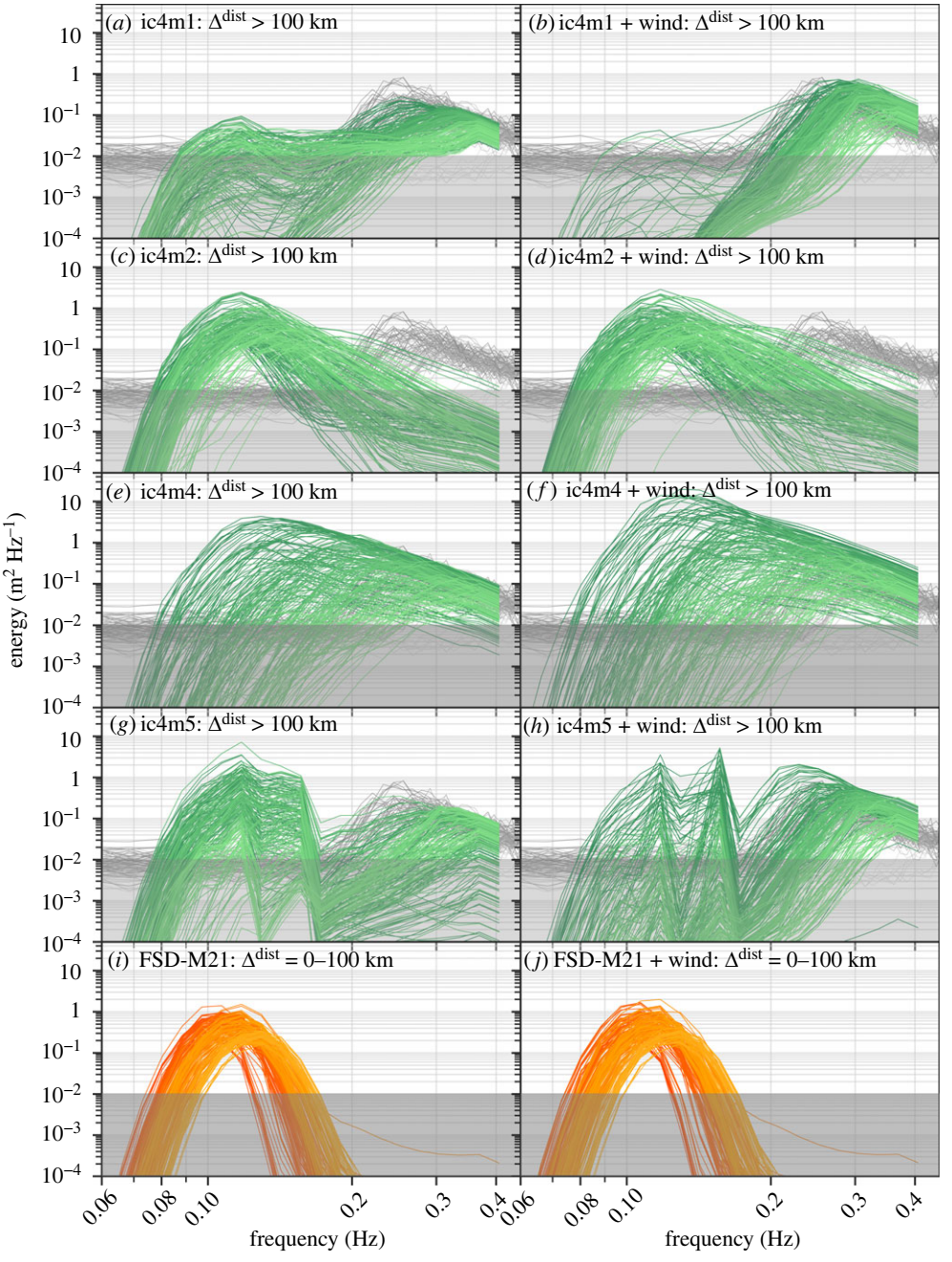


**Figure 6.** Hourly mean wave spectra from coupled wave-ice model experiments (green and orange) during July 2018 in the central Beaufort region surrounding the BGOS-SODA observations (latitudes 72°N to 79°N, longitudes 165°W to 130°W; see figure 1*c*). For visual clarity, plots show model spectra (coloured by peak frequency) from only 200 randomly selected grid cells when $H_s$ is greater than 0.3 m. Each row is a different attenuation scheme corresponding to those in table 2. Left column represents the standard experimental set-up (wind input declining to zero as SIC approaches 100%). Right column represents experiments with enhanced wind input (wind input declining to 50% as SIC approaches 100%). Bottom panels *i*, *j* (orange) show the first 0–100 km because there are no model spectra with $H_s > 0.3$ m beyond 100 km $\Delta^{dist}$ in the FSD-M21 case. BGOS-SODA observations from July (all years) beyond 100 km are shown in grey. No observations are available in July from the first 0–100 km (*i*, *j*). Grey shading below $10^{-2}$ represents approximate detection limit of BGOS-SODA instruments, included for reference. Results are not sensitive to random sampling of spectra (electronic supplementary material, figure S3).

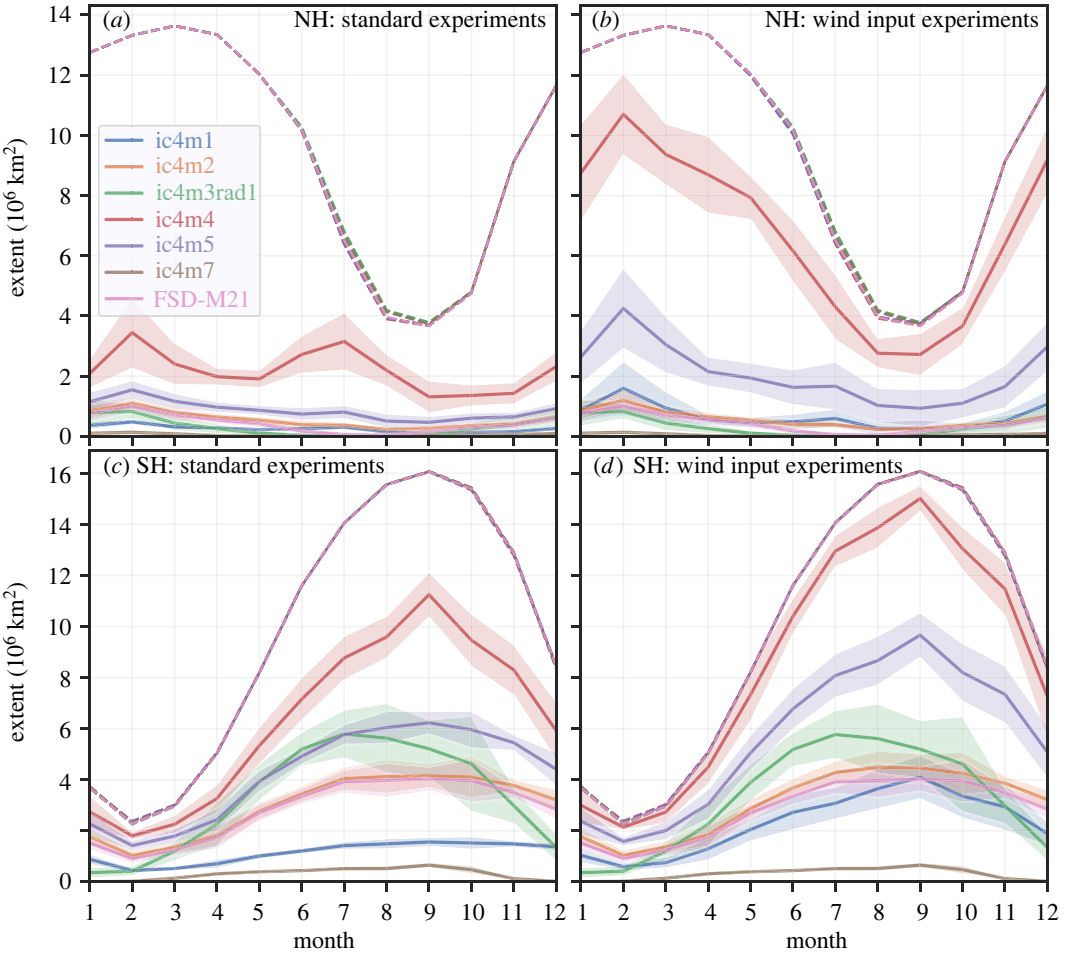


**Figure 7.** 2018 monthly means of daily wave-affected extent (solid lines) and sea ice extent (dashed lines) in global coupled wave-ice model experiments: (*a*,*b*) Northern Hemisphere and (*c*,*d*) Southern Hemisphere. Left column represents the standard experimental set-up (wind input declining to zero as SIC approaches 100%). Right column represents experiments with enhanced wind input (wind input declining to 50% as SIC approaches 100%). Coloured shading represents $\pm 1$ s.d. of the daily wave-affected extent computed for each month. (Online version in colour.)

In summary, the different attenuation schemes produce a wide range of spectral shapes in the July 2018 Beaufort Sea. A weak high-frequency attenuation rate (e.g. IC4M1 and IC4M5) permits the development of local wind waves beyond 100 km $\Delta^{\text{dist}}$ that resemble the observations. Spectra from the simple scheme of IC4M1 with enhanced wind input most closely resemble the observed spectra in this model.

## (c) Simulated wave-affected extent across polar oceans

Recent studies have started using the area of sea ice where ocean surface waves are present as a metric for model evaluation (e.g. [56]). Here, we investigate how uncertainty in wave-ice physics impacts the simulation of wave-affected extent across hemispheres and seasons. We compute the wave-affected extent as the total ocean area with SIC greater than 15% and $H_s > 0.3$ m (the threshold of detection that is applied in the BGOS-SODA observations). The spread in wave-affected extent between the attenuation schemes is substantial in both the Northern and the Southern Hemispheres (figure 7).

In the Arctic (figure 7*a*,*b*), schemes with the strongest attenuation result in a near-zero wave-affected extent during part of the summer season. Weaker attenuation rates yield non-trivial wave-affected extents even in the summer. The additional wind input (figure 7*b*) has a major impact on the weakest attenuation rates—more than doubling the wave extent for IC4M4 and IC4M5—but the schemes with strong damping of high-frequency energy are relatively unaffected. IC4M1 (which most closely resembles BGOS-SODA observations in the Beaufort Sea) shows a substantial increase in wave-affected extent when wind input is enhanced.

In the Southern Hemisphere (figure 7*c*,*d*), the spread between the schemes is larger than in the Arctic. During the summer minimum ice extent, the wave-affected extent ranges from near-complete coverage of all sea ice (IC4M4) to near-zero coverage (IC4M7). All methods besides IC4M7 have substantial waves throughout most of the year. IC4M1 has a relatively low wave-affected extent compared to other attenuation schemes even when supplied with additional wind input. This is because IC4M1 has strong attenuation of the longest swells. IC4M3 has relatively high wave-affected extent in the Antarctic winter compared to the other schemes, whereas it has a relatively low extent in the Arctic winter—this asymmetry is due to its weak attenuation of only the longest swells and strong attenuation at all shorter wavelengths.

Across the polar oceans, changing the model's attenuation scheme can have substantial impacts on the spatial extent of wave activity in sea ice. When the high-frequency attenuation of a given method is relatively weak, allowing additional wind input for wave generation also has a large impact on wave-affected extent. For some attenuation schemes (e.g. IC4M7, IC4M3rad1 and FSD-M21), the high-frequency damping is so strong in ice that the additional wind input cannot overcome it.

## 4. Discussion

Local wind waves that are generated far inside the MIZ may have impacts on sea ice evolution and ocean mixing that have not been investigated. Wind waves could enhance ice melt through overwash—occurring when waves cause water to spill over the edge of an ice floe—which is an active area of research [57,58]. If local waves are strong enough to cause fracture, they could reduce sea ice to small floe sizes. Lateral melt begins to play a critical role in Arctic summer conditions when the floe diameter is less than 30 m [59]. The vast majority of local wind-wave observations beyond 100 km $\Delta^{\mathrm{dist}}$ occur in July when the seasonal ice zone retreats over the mooring locations (distribution of samples by month is provided in the electronic supplementary material, figure S4). The SAR images in figure 5—along with observations of local wind waves—took place during a melt event in July 2018. A possible role for local waves in ice melt should be investigated further and considered in sea ice and climate model development.

Thus far, the quantitative impact of local wind waves on the sea ice floe size distribution remains unclear. According to the wave fracture parametrization in [33] (which is used by the model [3] in this study), a number of the observed wind-wave spectra have sufficient energy to cause wave fracture, producing floes of $O(10)$ metres (electronic supplementary material, figure S7) where lateral melt would be important. However, in the coupled wave-ice model experiments that show local wind-wave spectra in the Beaufort Sea (e.g. IC4M1, figure 6*a*,*b*), this parametrization results in simulated floe sizes that are unrealistically small across the polar oceans—IC4M1 has mean floe radii of 15 m (Arctic) and 7 m (Antarctic) at the end of the experiment (not shown). The current implementation does not include subgrid-scale attenuation, which may be important for short wind waves simulated on large spatial scales. An alternative wave fracture parametrization from [60] only permits waves longer than 5 s to fracture sea ice, but that restriction is due to a lower limit on floe diameter (set at 20 m). High-frequency waves have not been a focus of fracture parametrizations. High-temporal-resolution observations of the floe size distribution during wave fracture events are required to further develop our understanding and inform modifications to these parametrizations.

If future work suggests that local wind waves are important for climate-scale modelling—through their impact on ice fracture or other processes—there are various ways to improve their

representation in coarse-resolution models. These could include modifications to WW3 (such as extending the resolved frequency range and investigating alternative attenuation schemes), subgrid-scale parametrizations of fetch-limited wave generation and attenuation, and machine-learning emulation of very-high-resolution simulations or discrete element models that explicitly represent more of the relevant processes. At the spatial resolution required for climate-scale modelling, we cannot resolve the observed heterogeneity of the ice cover, and there will be compensating errors in subgrid-scale processes. For example, in our simulations, enhanced wind input may help to compensate for overestimated SIC (see SIC differences in electronic supplementary material, figure S5). The representation of wave-ice physics and parametrizations suited to climate-scale models may therefore differ from those suited to high-resolution models, and reconciling these differences will be an ongoing challenge as wave-ice interactions are included in coupled models (e.g. [61]) used for climate projections.

## 5. Conclusion

In this study, we first investigate wave spectra in a multi-year dataset (BGOS-SODA) from five subsurface moorings in the Beaufort Sea under seasonal ice cover. Between the sea ice edge and 100 km inside it, observations show a range of peak frequencies, representing a mixture of wind waves and swell. Beyond 100 km, the vast majority of waves measured (96 of 98 records) appear to be local wind waves following the fetch-limited power law for local wind-wave generation, and all 98 spectra have significant wave heights less than 1 m. We infer that these wind waves are generated over short distances (typically less than 20 km) in patches of open water amid partial ice cover, and they are observed in summer.

Secondly, we examine the impact of varying wave-ice physics in a global coupled wave-ice model. The model can capture broad characteristics of the BGOS-SODA observations beyond 100 km inside the ice edge (with a focus on July 2018) in climate-scale experiments that vary wave attenuation and wind input in ice. A weak high-frequency attenuation rate (as in the IC4M1 scheme) is required to simulate local wind waves, and the agreement with observations in this model is stronger when additional wind input for wave generation is permitted in high concentrations of sea ice. Several attenuation schemes investigated here show swell waves at large distances inside the sea ice edge, which are not supported by BGOS-SODA observations in the Beaufort Sea. Globally, we find that changing the attenuation scheme has a remarkable impact on the spatial extent of waves in ice. Increasing the wind input in ice can have a pronounced effect, but only when the attenuation rate of high frequencies is relatively weak.

Local wind waves in partial sea ice cover may act to enhance melting during the seasonal ice retreat by the fracturing of sea ice into small floes (of diameter less than approximately 30 m), overwash, ocean mixing and eddy generation. However, these mechanisms remain uncertain and require further observation and investigation. In particular, this work motivates reconsideration of how high-frequency waves should be treated in fracture parametrizations for climate models. Representing complex small-scale interactions between waves and sea ice in climate-scale models is a formidable challenge, but these efforts may be necessary to improve the simulation of sea ice variability and trends [3,38,62]. Observational constraints on large-scale features (such as the wave-affected extent) and on small-scale features (such as the spectral shape of waves in sea ice and the floe size distribution across seasons and basins) will all be required to advance parametrizations of wave-ice physics in the next generation of climate models.

Data accessibility. BGOS data were collected and made available by the Beaufort Gyre Exploration Program at Woods Hole Oceanographic Institution in collaboration with Fisheries and Oceans Canada at the Institute of Ocean Sciences. The BGOS datasets used in this study are available at digital.lib.washington.edu/researchworks/handle/1773/46260. The SODA data are available at digital.lib.washington.edu/researchworks/handle/1773/46919. SWIFT buoy data were collected by the Arctic Sea State programme and are available at www.apl.uw.edu/swift. NOAA/NSIDC Climate Data Record of SIC estimates are available at nsidc.org/data/G02202. The model output is available at https://doi.org/10.5281/zenodo.6213441 (IC4M1) [67], https://doi.org/10.5281/zenodo.6213793 (IC4M2) [68], https://doi.org/10.5281/zenodo.

6214364 (IC4M3rad1) [69], https://doi.org/10.5281/zenodo.6214555 (IC4M4) [70], https://doi.org/10.5281/zenodo.6214998 (IC4M5) [71], https://doi.org/10.5281/zenodo.6212423 (IC4M7) [72] and https://doi.org/10.5281/zenodo.6212232 (FSD-M21) [73]. The model code is available at github.com/ESCOMP/cesm, github.com/lettie-roach/CESM_CICE5 and github.com/vtcooper/WW3-CESM.

Electronic supplementary material is available online [74].

Authors' contributions. V.T.C.: conceptualization, data curation, formal analysis, funding acquisition, investigation, methodology, software, visualization, writing—original draft, writing—review and editing; L.A.R.: conceptualization, formal analysis, funding acquisition, investigation, methodology, software, supervision, writing—original draft, writing—review and editing; J.T.: conceptualization, data curation, funding acquisition, investigation, methodology, supervision, writing—review and editing; S.D.B.: data curation, funding acquisition, investigation, methodology, writing—review and editing; M.M.S.: funding acquisition, investigation, writing—review and editing; M.H.M.: investigation, writing—review and editing; C.M.B.: conceptualization, formal analysis, funding acquisition, investigation, methodology, resources, software, supervision, writing—review and editing.

All authors gave final approval for publication and agreed to be held accountable for the work performed therein.

Conflict of interest declaration. We declare we have no competing interests.

Funding. V.T.C. thanks the US Deptartment of Defense and Office of Naval Research (ONR) for support through a National Defense Science and Engineering Graduate Fellowship. This work was supported by the US National Science Foundation (NSF) grant no. OPP-1643431 (V.T.C., L.A.R., C.M.B.), the New Zealand Ministry of Business, Innovation and Employment—Science Investment Contract C01X1914 (L.A.R.), ONR grant no. N00014-16-1-2349 (J.T.), ONR grant no. N00014-18-1-2687 (S.D.B.), and NSF grant nos OPP-1724467 and OPP-1724748 (M.M.S).

Acknowledgements. V.T.C. thanks Mark Orzech, W. Erick Rogers, Craig Lee, David Bailey and Luke Bennetts for insightful discussions. SAR images are provided by Sentinel-1A/B SAR-C, EW Data, available through EO Browser using the script SAR-Ice © 2020 Martin Raspaud. High-performance computing support was provided by Cheyenne (doi:10.5065/D6RX99HX) through NCAR's Computational and Information Systems Laboratory, sponsored by the NSF.

## Appendix A. Non-dimensional scaling for wind-generated ocean waves

To interpret wave statistics, we employ non-dimensional scaling for wind-generated waves following [51]. These relations enable separation of wind waves from swell and provide estimates of the implied fetch for observed wind waves in partial ice cover. We calculate the following non-dimensional variables for the wave energy $E$, frequency $F$ and fetch distance $X$:

$$E = \left(\frac{gH_s}{4U_{10}^2}\right)^2, \quad F = \frac{f_p U_{10}}{g} \quad \text{and} \quad X = \frac{gx}{U_{10}^2}, \tag{A 1}$$

where $g$ is the gravitational acceleration; $U_{10}$ is the 10 m wind speed at the location of each *in situ* observation and model grid cell from JRA-55 reanalysis [29,30]; $H_s$ is the significant wave height, defined as $4\sqrt{\int E(f)\,\mathrm{d}f}$; $f_p$ is the peak frequency; and $x$ is the fetch, i.e. the distance over which waves are generated by local winds. Values of $H_s$ and $f_p$ are measured *in situ* and provided in model output. The fetch $x$ is not measured but rather inferred for specific wind waves as described below; we refer to this variable as the implied fetch.

In the marginal sea region of the observations considered, wave generation is generally limited by fetch rather than wind duration [1,63]. Several studies have developed empirical estimates of power laws for $E$ versus $X$ and $F$ versus $X$ that describe wind-generated waves in a fetch-limited regime. In [51] these estimates were combined into the relations

$$E = (7.5 \pm 2.0) \times 10^{-7} X^{0.8} \tag{A 2}$$

and

$$F = (2.0 \pm 0.3) X^{-0.25}, \tag{A 3}$$

which apply at least until reaching a fully developed limit for pure wind seas at $E_{\max} = (3.6 \pm 0.9) \times 10^{-3}$ and $F_{\min} = 0.13 \pm 0.02$. Using equation (A 1), we reformulate these power laws in

terms of the variables available from measurements and modelling, $E$ and $F$:

$$E = (6.9 \pm 3.8) \times 10^{-6} F^{-3.2}. \tag{A 4}$$

We identify waves that are accurately described by fetch-limited local wind generation, i.e. wind waves, as those that fall within the uncertainty bounds of the line defined by the power law in equation (A 4). If a spectrum has less energy $E$ than predicted by the wind-wave power law for a given frequency $F$ and it has a wave age greater than 1, we determine that the spectrum represents swell, i.e. long-period waves produced by non-local winds.

Wave age, a non-dimensional parameter $c/U$ defined by the ratio of the dominant phase speed $c_p$ to the wind speed $U_{10}$, can also distinguish swell from local wind waves. We take $c_p = g/(2\pi f_p)$ following the deep-water limit for surface gravity waves. When the wave age exceeds 1, waves travel faster than the winds. We note that the wave age can be expressed in terms of $F$ using equation (A 1) such that $c/U = (2\pi F)^{-1}$, and the wave age is greater than 1 when $F$ is less than $1/(2\pi)$.

Taking only the spectra that appear to be fetch-limited local wind waves (based on equation (A 4) and wave age), we can calculate an implied fetch $x$ corresponding to each wind-wave spectrum. This dimensional variable $x$ is recovered by solving for the non-dimensional $X$ in equation (A 2) or (A 3) based on the measured energy $E$ or frequency $F$, respectively, and then using equation (A 1) to restore the dimension. The implied fetch is an estimate of the open-water distance that would be required for local winds to generate a given wind-wave spectrum.

## Appendix B. Wind-speed estimates from the equilibrium range

Surface wind speed can be estimated from the equilibrium range in the high-frequency end of the wave spectrum (the 'spectral tail'). The equilibrium range is the portion of the wave spectrum where the source terms—wind input, nonlinear transfer and dissipation—are balanced [64]. We follow the methods from [54,55] that calculate a friction velocity $u_*$ by assuming $E(f) \propto u_* f^{-4}$, where $E(f)$ is energy and $f$ is frequency. This process begins with

$$E(f) = E_0 f^{-4}, \quad \text{where } E_0 = \frac{4g\beta I_p u_*}{(2\pi)^3}, \tag{B 1}$$

and we compute $E_0$ as the mean of $f^4 E(f)$ for the frequencies in the equilibrium range. The equilibrium range is identified as the 20 consecutive frequencies (all higher than $f_p$, up to a maximum of 0.5 Hz) that minimize standard error on the fit to $f^{-4}$. We require a minimum of 10 data points in the equilibrium range. The constant $\beta$ is an empirical constant that is set to 0.009 based on results in [55]; $I_p$ adjusts for directional spreading of waves and ranges from 1.9 (wide) to 3.1 (narrow) [65] with a typical value of 2.5 [54]. For observations beyond 100 km $\Delta^{\text{dist}}$, we use $I_p = 1.9$, expecting that directional spreading may be elevated in partial ice cover. For observations in open water, we use the typical value of $I_p = 2.5$.

We then have an estimate of $u_*$ which we can relate to the 10 m wind speed $U_{10}$ by assuming a logarithmic wind profile in the boundary layer,

$$U(z) = \frac{u_*}{\kappa} \ln\left(\frac{z}{z_0}\right), \tag{B 2}$$

with the von Karman constant $\kappa = 0.41$, $z = 10$ m, and ocean surface roughness length $z_0$. This is assumed to follow the Charnock relation [66],

$$z_0 = \frac{\alpha u_*^2}{g}, \tag{B 3}$$

although the presence of ice may affect $z_0$, introducing some additional uncertainty. Following eqn (16) in [55], $\alpha$ is determined by wave age according to

$$\alpha = 0.14 \left(\frac{u_*}{c_p}\right)^{0.61}, \tag{B 4}$$

where $c_p$ is the phase speed at the peak frequency. With these assumptions, we can estimate $U_{10}$ from the $E(f)$ measured by BGOS-SODA subsurface moorings, which are located roughly 30–45 m beneath the ocean surface.

## References


1. Thomson J, Rogers WE. 2014 Swell and sea in the emerging Arctic Ocean. *Geophys. Res. Lett.* **41**, 3136–3140. (doi:10.1002/2014GL059983)
2. Asplin MG, Galley R, Barber DG, Prinsenberg S. 2012 Fracture of summer perennial sea ice by ocean swell as a result of Arctic storms. *J. Geophys. Res. Oceans* **117**, C06025. (doi:10.1029/2011JC007221)
3. Roach LA, Bitz CM, Horvat C, Dean SM. 2019 Advances in modeling interactions between sea ice and ocean surface waves. *J. Adv. Model. Earth Syst.* **11**, 4167–4181. (doi:10.1029/2019MS001836)
4. Boutin G, Lique C, Ardhuin F, Rousset C, Talandier C, Accensi M, Girard-Ardhuin F. 2020 Towards a coupled model to investigate wave–sea ice interactions in the Arctic marginal ice zone. *Cryosphere* **14**, 709–735. (doi:10.5194/tc-14-709-2020)
5. Shen HH. 2022 Wave-in-ice: theoretical bases and field observations. *Phil. Trans. R. Soc. A* **380**, 20210254. (doi:10.1098/rsta.2021.0254)
6. Thomson J. 2022 Wave propagation in the marginal ice zone: connections and feedback mechanisms within the air–ice–ocean system. *Phil. Trans. R. Soc. A* **380**, 20210251. (doi:10.1098/rsta.2021.0251)
7. Collins CO, Rogers WE, Marchenko A, Babanin AV. 2015 In situ measurements of an energetic wave event in the Arctic marginal ice zone. *Geophys. Res. Lett.* **42**, 1863–1870. (doi:10.1002/2015GL063063)
8. Stopa JE, Sutherland P, Ardhuin F. 2018 Strong and highly variable push of ocean waves on Southern Ocean sea ice. *Proc. Natl. Acad. Sci. USA* **115**, 5861–5865. (doi:10.1073/pnas.1802011115)
9. Brouwer J *et al.* 2022 Altimetric observation of wave attenuation through the Antarctic marginal ice zone using ICESat-2. *Cryosphere* **16**, 2325–2353. (doi:10.5194/tc-16-2325-2022)
10. Collard F, Marié L, Nouguier F, Kleinherenbrink M, Ehlers F, Ardhuin F. 2022 Wind-wave attenuation in Arctic sea ice: a discussion of remote sensing capabilities. *J. Geophys. Res. Oceans* **127**, e2022JC018654. (doi:10.1029/2022JC018654)
11. Squire VA. 2020 Ocean wave interactions with sea ice: a reappraisal. *Annu. Rev. Fluid Mech.* **52**, 37–60. (doi:10.1146/annurev-fluid-010719-060301)
12. Perrie W, Meylan MH, Toulany B, Casey MP. 2022 Modelling wave–ice interactions in three dimensions in the marginal ice zone. *Phil.Trans. R. Soc. A* **380**, 20210263. (doi:10.1098/rsta.2021.0263)
13. Rogers WE, Meylan MH, Kohout AL. 2021 Estimates of spectral wave attenuation in Antarctic sea ice, using model/data inversion. *Cold Reg. Sci. Technol.* **182**, 103198. (doi:10.1016/j.coldregions.2020.103198)
14. Ardhuin F, Otero M, Merrifield S, Grouazel A, Terrill E. 2020 Ice breakup controls dissipation of wind waves across Southern Ocean sea ice. *Geophys. Res. Lett.* **47**, e2020GL087699. (doi:10.1029/2020GL087699)
15. Squire VA, Moore SC. 1980 Direct measurement of the attenuation of ocean waves by pack ice. *Nature* **283**, 365–368. (doi:10.1038/283365a0)
16. Masson D, Leblond PH. 1989 Spectral evolution of wind-generated surface gravity waves in a dispersed ice field. *J. Fluid Mech.* **202**, 43–81. (doi:10.1017/S0022112089001096)
17. Smith M, Thomson J. 2016 Scaling observations of surface waves in the Beaufort Sea. *Elementa* **4**, 000097. (doi:10.12952/journal.elementa.000097)
18. Liu Q, Rogers WE, Babanin A, Li J, Guan C. 2020 Spectral modeling of ice-induced wave decay. *J. Phys. Oceanogr.* **50**, 1583–1604. (doi:10.1175/JPO-D-19-0187.1)
19. Krishfield RA, Proshutinsky A, Tateyama K, Williams WJ, Carmack EC, McLaughlin FA, Timmermans ML. 2014 Deterioration of perennial sea ice in the Beaufort Gyre from 2003 to 2012 and its impact on the oceanic freshwater cycle. *J. Geophys. Res. Oceans* **119**, 1271–1305. (doi:10.1002/2013JC008999)

20. Herbers THC, Jessen PF, Janssen TT, Colbert DB, MacMahan JH. 2012 Observing ocean surface waves with GPS-tracked buoys. *J. Atmos. Oceanic Technol.* **29**, 944–959. (doi:10.1175/JTECH-D-11-00128.1)
21. Kuik AJ, van Vledder GP, Holthuijsen LH. 1988 A method for the routine analysis of pitch-and-roll buoy wave data. *J. Phys. Oceanogr.* **18**, 1020–1034. (doi:10.1175/1520-0485(1988)018<1020:AMFTRA>2.0.CO;2)
22. Thomson J, Girton JB, Jha R, Trapani A. 2018 Measurements of directional wave spectra and wind stress from a wave glider autonomous surface vehicle. *J. Atmos. Oceanic Technol.* **35**, 347–363. (doi:10.1175/JTECH-D-17-0091.1)
23. Thomson J. 2020 *Long-term measurements of ocean waves and sea ice draft in the central Beaufort Sea.* Technical Memorandum APL-UW TM 1-20. Seattle, WA: Applied Physics Laboratory, University of Washington.
24. Brenner S, Rainville L, Thomson J, Cole S, Lee C. 2021 Comparing observations and parameterizations of ice-ocean drag through an annual cycle across the Beaufort Sea. *J. Geophys. Res. Oceans* **126**, e2020JC016977. (doi:10.1029/2020JC016977)
25. Sentinel Hub. *EO Browser.* See https://apps.sentinel-hub.com/eo-browser.
26. Raspaud M, Itkin M. *SAR-Ice: a sea ice RGB composite*. See https://custom-scripts.sentinel-hub.com/sentinel-1/sar-ice/.
27. Hunke EC, Lipscomb WH, Turner AK, Jeffery N, Elliot S. 2015 *CICE: the Los Alamos sea ice model documentation and software user's manual version 5.1.* Technical Report LA-CC-06-012. Los Alamos, NM: Los Alamos National Laboratory.
28. The WAVEWATCH III® Development Group (WW3DG). 2016 *User manual and system documentation of WAVEWATCH III® version 5.16*. College Park, MD: NOAA/NWS/NCEP/MMAB.
29. Kobayashi S *et al.* 2015 The JRA-55 reanalysis: general specifications and basic characteristics. *J. Meteorol. Soc. Jpn. Ser. II* **93**, 5–48. (doi:10.2151/jmsj.2015-001)
30. Japan Meteorological Agency. 2013 JRA-55: Japanese 55-year reanalysis, daily 3-hourly and 6-hourly data. Boulder, CO: Research Data Archive at the National Center for Atmospheric Research, Computational and Information Systems Laboratory. (doi:10.5065/D6HH6H41)
31. Bitz CM, Shell KM, Gent PR, Bailey DA, Danabasoglu G, Armour KC, Holland MM, Kiehl JT. 2012 Climate sensitivity of the community climate system model, version 4. *J. Clim.* **25**, 3053–3070. (doi:10.1175/JCLI-D-11-00290.1)
32. Roach LA, Horvat C, Dean SM, Bitz CM. 2018 An emergent sea ice floe size distribution in a global coupled ocean-sea ice model. *J. Geophys. Res. Oceans* **123**, 4322–4337. (doi:10.1029/2017JC013692)
33. Horvat C, Tziperman E. 2015 A prognostic model of the sea-ice floe size and thickness distribution. *Cryosphere* **9**, 2119–2134. (doi:10.5194/tc-9-2119-2015)
34. Horvat C, Roach LA. 2022 WIFF1.0: a hybrid machine-learning-based parameterization of wave-induced sea ice floe fracture. *Geosci. Model Dev.* **15**, 803–814. (doi:10.5194/gmd-15-803-2022)
35. Wadhams P, Squire VA, Goodman DJ, Cowan AM, Moore SC. 1988 The attenuation rates of ocean waves in the marginal ice zone. *J. Geophys. Res.* **93**, 6799–6818. (doi:10.1029/JC093iC06p06799)
36. Meylan MH, Bennetts LG, Kohout AL. 2014 In situ measurements and analysis of ocean waves in the Antarctic marginal ice zone. *Geophys. Res. Lett.* **41**, 5046–5051. (doi:10.1002/2014GL060809)
37. Kohout AL, Meylan MH. 2008 An elastic plate model for wave attenuation and ice floe breaking in the marginal ice zone. *J. Geophys. Res.* **113**, C09016. (doi:10.1029/2007JC004434)
38. Kohout AL, Williams MJM, Dean SM, Meylan MH. 2014 Storm-induced sea-ice breakup and the implications for ice extent. *Nature* **509**, 604–607. (doi:10.1038/nature13262)
39. Collins CO, Rogers WE. 2017. *A source term for wave attenuation by sea ice in WAVEWATCH III®: IC4*. Technical Report NRL/MR/7320-17-9726. Stennis Space Center, MS: United States Naval Research Laboratory.
40. Doble MJ, De Carolis G, Meylan MH, Bidlot J, Wadhams P. 2015 Relating wave attenuation to pancake ice thickness, using field measurements and model results. *Geophys. Res. Lett.* **42**, 4473–4481. (doi:10.1002/2015GL063628)

41. Meylan MH, Horvat C, Bitz CM, Bennetts LG. 2021 A floe size dependent scattering model in two- and three-dimensions for wave attenuation by ice floes. *Ocean Model.* **161**, 101779. (doi:10.1016/j.ocemod.2021.101779)
42. Rogers WE, Yu J, Wang DW. 2021 *Incorporating dependence on ice thickness in empirical parameterizations of wave dissipation by sea ice*. Technical Report NRL/OT/7320-21-5145. Stennis Space Center, MS: United States Naval Research Laboratory.
43. Stopa JE, Ardhuin F, Girard-Ardhuin F. 2016 Wave climate in the Arctic 1992–2014: seasonality and trends. *Cryosphere* **10**, 1605–1629. (doi:10.5194/tc-10-1605-2016)
44. Ardhuin F, Boutin G, Stopa J, Girard-Ardhuin F, Melsheimer C, Thomson J, Kohout A, Doble M, Wadhams P. 2018 Wave attenuation through an Arctic marginal ice zone on 12 October 2015: 2. Numerical modeling of waves and associated ice breakup. *J. Geophys. Res.: Oceans* **123**, 5652–5668. (doi:10.1002/2018JC013784)
45. Sutherland G, Rabault J, Christensen KH, Jensen A. 2019 A two layer model for wave dissipation in sea ice. *Appl. Ocean Res.* **88**, 111–118. (doi:10.1016/J.APOR.2019.03.023)
46. Rogers WE, Thomson J, Shen HH, Doble MJ, Wadhams P, Cheng S. 2016 Dissipation of wind waves by pancake and frazil ice in the autumn Beaufort Sea. *J. Geophys. Res.: Oceans* **121**, 7991–8007. (doi:10.1002/2016JC012251)
47. Polnikov VG, Lavrenov IV. 2007 Calculation of the nonlinear energy transfer through the wave spectrum at the sea surface covered with broken ice. *Oceanology* **47**, 334–343. (doi:10.1134/S0001437007030058)
48. Meier WN, Fetterer F, Savoie M, Mallory S, Duerr R, Stroeve J. 2017 *NOAA/NSIDC climate data record of passive microwave sea ice concentration, version 3*. Data set G02202. Boulder, CO: National Snow and Ice Data Center. See https://nsidc.org/data/g02202/versions/3.
49. Peng G, Meier WN, Scott DJ, Savoie MH. 2013 A long-term and reproducible passive microwave sea ice concentration data record for climate studies and monitoring. *Earth Syst. Sci. Data* **5**, 311–318. (doi:10.5194/essd-5-311-2013)
50. Meier WN, Fetterer F, Windnagel AK, Stewart JS. 2021 *NOAA/NSIDC climate data record of passive microwave sea ice concentration, version 4*. Data set G02202. Boulder, CO: National Snow and Ice Data Center. See https://nsidc.org/data/g02202/versions/4.
51. Young IR. 1999 *Wind generated ocean waves*. Oxford, UK: Elsevier.
52. Thomson J, Hošeková L, Meylan MH, Kohout AL, Kumar N. 2021 Spurious rollover of wave attenuation rates in sea ice caused by noise in field measurements. *J. Geophys. Res. Oceans* **126**, e2020JC016606. (doi:10.1029/2020JC016606)
53. Thomson J *et al.* 2018 Overview of the Arctic Sea State and Boundary Layer Physics program. *J. Geophys. Res. Oceans* **123**, 8674–8687. (doi:10.1002/2018JC013766)
54. Thomson J, D'Asaro EA, Cronin MF, Rogers WE, Harcourt RR, Shcherbina A. 2013 Waves and the equilibrium range at Ocean Weather Station P. *J. Geophys. Res. Oceans* **118**, 5951–5962. (doi:10.1002/2013JC008837)
55. Voermans JJ, Smit PB, Janssen TT, Babanin AV. 2020 Estimating wind speed and direction using wave spectra. *J. Geophys. Res. Oceans* **125**, 1–16. (doi:10.1029/2019JC015717)
56. Boutin G, Williams T, Horvat C, Brodeau L. 2022 Modelling the Arctic wave-affected marginal ice zone: a comparison with ICESat-2 observations. *Phil. Trans. R. Soc. A* **380**, 20210262. (doi:10.1098/rsta.2021.0262)
57. Nelli F, Bennetts LG, Skene DM, Toffoli A. 2020 Water wave transmission and energy dissipation by a floating plate in the presence of overwash. *J. Fluid Mech.* **889**, A19. (doi:10.1017/jfm.2020.75)
58. Passerotti G, Bennetts LG, von Bock und Polach F, Alberello A, Puolakka O, Dolatshah A, Monbaliu J, Toffoli A. 2022 Interactions between irregular wave fields and sea ice: a physical model for wave attenuation and ice breakup in an ice tank. *J. Phys. Oceanogr.* **52**, 1431–1446. (doi:10.1175/JPO-D-21-0238.1)
59. Steele M. 1992 Sea ice melting and floe geometry in a simple ice-ocean model. *J. Geophys. Res. Oceans* **97**, 17 729–17 738. (doi:10.1029/92JC01755)
60. Williams TD, Bennetts LG, Squire VA, Dumont D, Bertino L. 2013 Wave-ice interactions in the marginal ice zone. Part 1: theoretical foundations. *Ocean Model.* **71**, 81–91. (doi:10.1016/j.ocemod.2013.05.010)
61. Danabasoglu G *et al.* 2020 The Community Earth System Model version 2 (CESM2). *J. Adv. Model. Earth Syst.* **12**, e2019MS001916. (doi:10.1029/2019MS001916)

62. Bateson AW, Feltham DL, Schröder D, Hosekova L, Ridley JK, Aksenov Y. 2020 Impact of sea ice floe size distribution on seasonal fragmentation and melt of Arctic sea ice. *Cryosphere* **14**, 403–428. (doi:10.5194/tc-14-403-2020)
63. Hasselmann K *et al*. 1973 *Measurements of wind-wave growth and swell decay during the Joint North Sea Wave Project (JONSWAP)*. Hamburg, Germany: Deutsches Hydrographisches Institut.
64. Phillips OM. 1985 Spectral and statistical properties of the equilibrium range in wind-generated gravity waves. *J. Fluid Mech.* **156**, 505–531. (doi:10.1017/S0022112085002221)
65. Juszko BA, Marsden RF, Waddell SR. 1995 Wind stress from wave slopes using Phillips equilibrium theory. *J. Phys. Oceanogr.* **25**, 185–203. (doi:10.1175/1520-0485(1995)025<0185:WSFWSU>2.0.CO;2)
66. Charnock H. 1955 Wind stress on a water surface. *Q. J. R. Meteorol. Soc.* **81**, 639–640. (doi:10.1002/qj.49708135027)
67. Cooper VT. 2022 ic4m1 [Data set]. *Zenodo*. (doi:10.5281/zenodo.6213441)
68. Cooper VT. 2022 ic4m2 [Data set]. *Zenodo*. (doi:10.5281/zenodo.6213793)
69. Cooper VT. 2022 ic4m3rad1 [Data set]. *Zenodo*. (doi:10.5281/zenodo.6214364)
70. Cooper VT. 2022 ic4m4. *Zenodo*. (doi:10.5281/zenodo.6214555)
71. Cooper VT. 2022 ic4m5 [Data set]. *Zenodo*. (doi:10.5281/zenodo.6214998)
72. Cooper VT. 2022 ic4m7 [Data set]. *Zenodo*. (doi:10.5281/zenodo.6212423)
73. Cooper VT. 2022 FSD-scatter [Data set]. *Zenodo*. (doi:10.5281/zenodo.6212232)
74. Cooper VT. 2022 Wind waves in sea ice of the western Arctic and a global coupled wave-ice model. Figshare. (doi:10.6084/m9.figshare.c.6135513)